



High-resolution surface salinity maps in coastal oceans based on geostationary ocean color images: quantitative analysis of river plume dynamics

Satoshi Nakada¹ · Shiho Kobayashi² · Masataka Hayashi³ · Joji Ishizaka⁴ · Satoshi Akiyama⁵ · Masaki Fuchi⁶ · Masaki Nakajima⁵

Received: 18 May 2017 / Revised: 15 December 2017 / Accepted: 16 December 2017 / Published online: 15 January 2018
© The Oceanographic Society of Japan and Springer Japan KK, part of Springer Nature 2018, corrected publication 2021

Abstract

Sea surface salinity (SSS) in coastal oceans is a direct indicator of riverine plumes and provides essential information about the ocean environment and ecosystem, which affects coastal fisheries, aquaculture, and marine harvests. However, to accurately capture SSS patterns in coastal oceans, high temporal and spatial resolutions are required. This paper introduces a methodology to produce high-resolution (~ 500 m) SSS maps for analysis of river plumes in coastal oceans based on hourly chromophoric dissolved organic matter data collected by the Geostationary Ocean Color Imager. Osaka Bay, located in the eastern Seto Inland Sea, was selected as a pilot region. A comparison between the initial estimates and calibrated SSS data showed a substantial decrease in estimation error, by up to 71%, over a wide range of salinity (20–34) using in situ SSS data collected through an automated observation system. Calculating the salinity anomaly based on the SSS map to identify plume areas, we evaluated the impact of a large runoff event induced by a super typhoon on the river plumes. After the plume formed in the estuary, it extended southward to the bay mouth along the southeastern coast. The plume area during the post-typhoon period covered half of the bay, approximately 1.5 times the area during the pre-typhoon period. The post-typhoon, low-SSS period continued for approximately 2 weeks. Our approach can be of practical use for analyzing the dynamics of river plumes in coastal oceans, leading to the development of coastal ocean prediction models related to operational oceanography.

Keywords Sea surface salinity · Coastal oceans · Chromophoric dissolved organic matter · River plume · Typhoon · Geostationary ocean color satellite · Osaka Bay

Electronic supplementary material The online version of this article (<https://doi.org/10.1007/s10872-017-0459-4>) contains supplementary material, which is available to authorized users.

✉ Satoshi Nakada
snakada@maritime.kobe-u.ac.jp

Shiho Kobayashi
shihok@kais.kyoto-u.ac.jp

Masataka Hayashi
m-hayashi@sat-gis.co.jp

Joji Ishizaka
jishizaka@nagoya-u.jp

Satoshi Akiyama
AkiyamaS@o-suishi.zaqr.jp

Masaki Fuchi
mfuchi@maritime.kobe-u.ac.jp

Masaki Nakajima
NakajimaM@o-suishi.zaqr.jp

- 1 Graduate School of Maritime Science, Kobe University, 5-1-1 Fukae-minami, Higashi-nada-ku, Kobe 658-0022, Japan
- 2 Field Science Education and Research Center, Kyoto University, Kitashirakawa -Oiwake Cho, Sakyo-ku, Kyoto 606-8502, Japan
- 3 Science and Technology Co., Ltd., 3-9-2, Kobai-cho, Showa-ku, Nagoya, Aichi 466-0031, Japan
- 4 Institute for Space-Earth Environmental Research (ISEE), Nagoya University, Furo-cho, Chikusa-ku, Nagoya 464-8601, Japan
- 5 Research Institute of Environment, Agriculture and Fisheries, Osaka Prefecture, 2926-1 Tanigawa, Tanagawa, Misaki-cho, Sennan-gun, Osaka 599-0311, Japan
- 6 International Maritime Research Centre, Kobe University, 5-1-1 Fukae-minami, Higashi-nada-ku, Kobe 658-0022, Japan

1 Introduction

Riverine freshwater plumes in coastal oceans are crucial contributors to deposition, re-suspension, and transport of dissolved materials such as land-derived nutrients (e.g., Herbeck et al. 2011; Fichot et al. 2014). The riverine materials input to regions of freshwater influence (ROFI), which exist between oceans and estuaries (Simpson 1997), often yield significant fishery resources and may be associated with eutrophication in the river plume. The plume, which is characterized by low-salinity water from the estuary, can determine the water density structure and circulation system of these regions (Garvine 1999). Sea surface salinity (SSS) is a direct indicator of a freshwater plume associated with river discharge (Sasaki et al. 2008). Therefore, accurate SSS maps are essential to investigations of the ocean environment and ecosystems relevant to coastal fisheries, aquaculture, and marine harvests. This paper addresses the establishment of spatiotemporally high-resolution SSS maps to accurately analyze river plumes in coastal oceans based on ocean color products of geostationary satellites.

High-resolution SSS maps are urgently needed in marginal and coastal oceans to meet growing scientific and societal demands. For example, the low-salinity water formed by the Changjiang (Yangtze) River discharge is used as an index to predict the abundance of giant jellyfish (*Nemopilema nomurai*), thus affecting the efficiency of fishery operations (Kawahara et al. 2006). The abundance of these jellyfish is strongly correlated with riverine SSS along the coastal branch of the Tsushima Warm Current (Senjyu et al. 2013). In Funaka Bay, Japan, located in the subarctic Oyashio region, the river plume contains abundant nutrients from snowmelt runoff that can increase the biomass of phytoplankton associated with scallop fishery production (Nakada et al. 2014). Thus, SSS data can provide a practical index for aquaculture and fisheries, and holds similar significance for nori (*Porphyra*) production and discoloration in the Seto Inland Sea, Japan (e.g., Takagi et al. 2012), and the distribution, survival, and growth of commercial fishery resources such as oysters in the Chesapeake Bay, USA (Vogel and Brown 2016). From an oceanographic standpoint, SSS is primarily useful for detection of ocean currents and water masses, such as the East Sakhalin Current (Kuroda et al. 2014) and Coastal Oyashio Water in summer (Kusaka et al. 2013). SSS can be a representative indicator for hydrological factors, such as riverine freshwater input to the ocean associated with river plumes (e.g., Son et al. 2012) and evaporation and precipitation over the ocean (Lagerloef et al. 2008). In numerical and modeling studies, SSS can be used as input data to determine the surface boundary and initial

conditions, in addition to validation data for simulated SSS in an urbanized nearshore area with numerous landfills (Nakada et al. 2017). In particular, high-resolution SSS maps of the coastal oceans are essential for validating the SSS simulated by high-resolution coastal ocean models to improve model reproducibility (Nakada et al. 2012; Urakawa et al. 2015; Sakamoto et al. 2016).

To date, satellite-derived SSS datasets or maps have been established with global coverage based on microwave measurements (L-band radiometers), such as the Soil Moisture and Ocean Salinity (SMOS, European Space Agency, ESA) and Aquarius/SAC-D (National Aeronautics and Space Administration, NASA) missions to directly monitor salinity at the ocean surface (e.g., Lagerloef et al. 2008). Satellite-derived SSS data from current microwave sensors remains a limitation, as they cannot produce satisfactory resolution in coastal oceans (Bai et al. 2013) due to land contamination, coarse spatial resolution (typically 30–300 km), and long revisiting time (3 days or more; Koblinsky et al. 2003; Lagerloef et al. 2008; Font et al. 2010; Kerr et al. 2010). Neither mission was designed to observe SSS accurately in coastal regions with sufficient spatial and temporal resolution to monitor river plumes, because the SSS associated with a riverine plume exhibits high variation at small temporal and spatial scales. For example, the SSS distribution difference between pre- and post-typhoon samples can vary considerably due to the large amount of river runoff (Herbeck et al. 2011).

To estimate SSS with high resolution in coastal seas, two approaches employing satellite ocean color products can be used. Recent approaches directly apply ocean color data based on the neural networks method (Geiger et al. 2013), and utilize remote sensing reflectance data based on multiple statistical models (Urquhart et al. 2012; Qing et al. 2013). For these studies, use of satellite ocean color data in coastal areas can be prone to error due to the presence of multiple suspended constituents, including biogenic and terrigenous particles such as phytoplankton (Vogel and Brown 2016); to obtain accurate and real-time salinity estimated using those approaches, in situ ocean color datasets, such as remote sensing reflectance is necessary for sea parameter data ("sea truth") with appropriate spatial and temporal resolution.

The most frequently used approach is to utilize the linear relationship between SSS and the optical absorption coefficient of colored (or chromophoric) dissolved organic matter (a_{CDOM}), which has a significant negative correlation (e.g., Binding and Bowers 2003; Wouthuyzen et al. 2011). Chromophoric dissolved organic matter (CDOM) is soluble in riverine freshwater and rich in terrestrial plant-derived compounds but is made mostly of biologically recalcitrant substances (Hansell 2013). Therefore, CDOM can behave conservatively in estuaries or ROFIs, where physical mixing

prevails (Bowers and Brett 2008). In recent years, SSS has been empirically estimated from satellite-derived a_{CDOM} data based on the SSS–CDOM relationship in many river plume-dominated oceans, such as the outputs of the Amazon and Orinoco Rivers (e.g., Hu et al. 2004; Del Vecchio and Subramaniam 2004; Moller et al. 2010; Del Castillo et al. 1999), the Changjiang River (e.g., Sasaki et al. 2008; Bai et al. 2014), and the Mississippi River (Del Castillo and Miller 2008). However, these studies were based on daily satellite data and were limited to large ocean regions ($\sim 10^5 \text{ km}^2$) relative to the horizontal resolution ($\sim 1 \text{ km}$) of ocean color sensors such as NASA's Moderate Resolution Imaging Spectroradiometer (MODIS). In the coastal oceans, higher-resolution data are necessary to study oceanic phenomena that fluctuate in time and space, which are also difficult to elucidate using limited field surveys (Vogel and Brown 2016).

The Korean geostationary satellite Communication, Ocean and Meteorological Satellite (COMS), delivered by the Ariane 5 launch vehicle, was successfully launched in June 2010 from the Space Center in Kourou, French Guiana. The COMS carries the world's first geostationary ocean color sensor, the Geostationary Ocean Color Imager (GOCI), to measure radiance from the ocean surface in the visible and near-infrared bands. Observations from GOCI to COMS are available to easily derive high-resolution ($\sim 500 \text{ m}$) a_{CDOM} data, in addition to a higher temporal resolution (hourly) in daytime hours. These specifications are advantageous to observation of ocean color compared with other sensors.

This paper presents a novel methodology to produce high-resolution SSS maps based on GOCI products at the local scale ($\sim 10^3 \text{ km}^2$) in a semi-enclosed bay over a long-term period. Furthermore, this method can improve accuracy of SSS estimates by utilizing real-time in situ SSS data from an automated observation system. In this research, we first evaluated how this methodology can improve the accuracy of SSS datasets in conjunction with time series of hourly in situ SSS data. Then, SSS maps with high spatiotemporal resolution were produced to analyze seasonal SSS patterns and to quantify the river plume area. Finally, we analyzed the river plume dynamics induced by an extreme typhoon and the influence of this event on the decrease of SSS based on comprehensive analysis of hydrometeorological datasets.

2 Methods and materials

2.1 Study area setting

Osaka Bay, located in the eastern Seto Inland Sea of central Japan (Fig. 1), was selected as a pilot area for development of high-resolution SSS maps, because this area's distinct river plume can be expected to be induced by large runoff

events from the Yodo and Yamato Rivers. The estuaries of these rivers are located in the bay head. Osaka Bay has a sloped bottom topography with a diameter of about 55 km, a mean depth of approximately 20 m, and a surface area of 1450 km². The bay is connected with the northwestern Pacific Ocean via the Kitan Strait and Kii Channel at the southern bay mouth and with the Harima-Nada (Harima Sea) via the Akashi Strait at the western bay mouth. Although Osaka Bay is a typical semi-enclosed bay in Japan, the subtropical, warm, and saline Kuroshio water inflows intermittently into the bay through the southern bay mouth in an approximately 100-m-deep submarine valley (Yanagi 1996). Strong tidal currents mix the riverine low-salinity water with saline water originating from the Kuroshio through the Kitan Strait (Yanagi and Takahashi 1988a), resulting in a significant salinity gradient that increases from northeast to southwest with a salinity range of 10–35. Terrestrial water can remain in the bay for more than 2 months (Yanagi and Takahashi 1988b). These unique oceanographic features are crucial to management of fisheries resources such as flat-fishes and bivalves (e.g., Shigeta 2008).

The annual mean discharges of the Yodo and Yamato Rivers are 268 and 19 m³ s⁻¹, respectively, according to observed runoff data provided by the Ministry of Land, Infrastructure, Transport and Tourism of Japan (MLIT). The Yodo River drains a large catchment area (8240 km²), which contains a population of approximately 12 million. The Yamato River (Fig. 1) has the second largest watershed (1070 km²), but its discharge is approximately one tenth of that from the Yodo River (Yanagi 1980). These two rivers provide the greatest freshwater supply to Osaka Bay, contributing up to 95% of the bay's freshwater (Hoshika et al. 1994). Other rivers flowing into the bay have small watersheds, up to approximately 496 km² (Muko River). The annual mean discharge from all rivers into the bay is 443 m³ s⁻¹ (Yamamoto et al. 1996).

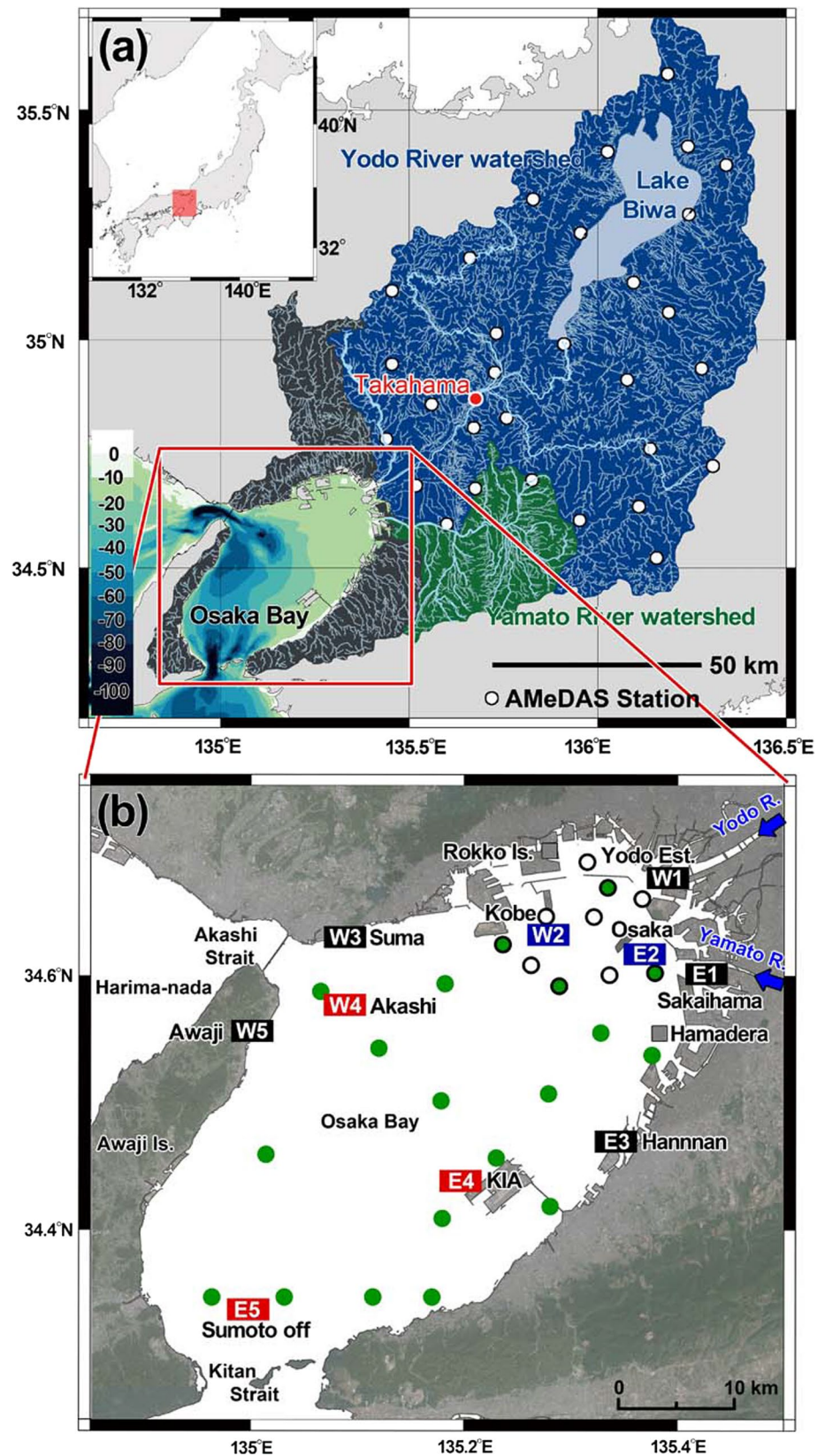
2.2 Data sources

2.2.1 Satellite ocean color radiometric measurements

GOCI–COMS obtains eight hourly images during the daytime and covers approximately 2500 × 2500 km² around the Japanese Islands and Korean Peninsula, centered at 36°N and 130°E with a spatial resolution of ca. 500 m and a very high signal-to-noise ratio (> 1000; Amin et al. 2013). The expected lifespan of the GOCI mission is 7 years.

GOCI has six visible bands, centered at 412, 443, 490, 555, 660, and 680 nm, and two near-infrared bands, centered at 745 and 865 nm. Level-1 products were downloaded from the website of the Korea Ocean Satellite Center (KOSC, http://kosc.kiost.ac/eng/p20/kosc_p21.html). We used the GOCI Data Processing System (GDPS) developed by the

Fig. 1 **a** Map of the study area showing watersheds and river paths flowing into Osaka Bay, which is located in the central region of the main island of Japan, indicated by the red-shaded square in the upper-left map. The color scale in the bay indicates depth in meters. Blue and green colors on land indicate the watersheds of the Yodo River and Yamato River, respectively. Red squares denote the area analyzed with satellite ocean color data. White dots represent Automated Meteorological Data Acquisition System (AMeDAS) stations, and the red dot represents the river observation station at Takahama. **b** Map of in situ observational stations and water sampling sites for $a_y(443)$. The green dots indicate stations regularly monitored by the Marine Fisheries Research Center, Research Institute of Environment, Agriculture and Fisheries, Osaka Prefectural Government (MFRC-OPG). Black circles indicate stations occasionally sampled by the Faculty of Maritime Sciences, Kobe University (FM-SKU). Rectangles indicate stations of the Observing System for Aquatic Quality at Automated Stations in the Osaka Bay (OSAQAS). The data collected at the stations denoted by the red and blue rectangles were used for calibration and validation of the satellite-derived SSS map, respectively. The data collected at stations marked by black rectangles were not used. Blue arrows indicate river flow inlets



Korea Institute of Ocean Science and Technology (Ryu et al. 2012) to obtain well-calibrated level-2 products converted from level-1 data. The algorithm used to estimate a_{CDOM} in the GDPS computes the absorption coefficient of dissolved organic matter at wavelength $\lambda = 400$ nm, using the remote sensing reflectance ratio of bands 1 (412 nm) to 4 (555 nm) with the equation, $a_{\text{CDOM}}(400) = 0.2355R^{-1.3423} \text{ m}^{-1}$, where $R = R_{\text{rs}}(412)/R_{\text{rs}}(555)$ (Moon et al. 2012). Pixel data of a_{CDOM} were extracted in the study area from 34.25°N to 34.75°N and 134.85°E to 135.5°E. The acquisition period for GOCI products was from April to September in 2015 and 2016, which includes a field survey period, explained below.

2.2.2 Field survey data acquisition

Observational data were obtained by the Marine Fisheries Research Center, Research Institute of Environment, Agriculture and Fisheries, Osaka Prefectural Government (MFRC-OPG), and the Faculty of Maritime Sciences, Kobe University (FMS-KU) in four seasons from 2015 to 2016 (Table 1). MFRC-OPG makes regular observations for water temperature, salinity, and other factors collected using R/V Osaka by casting multiple water quality sensors (RINKO Profiler ASTD102; JFE Advantec Co., Ltd., Nishinomiya) at 20 fixed stations distributed throughout the bay (Fig. 1). Additionally, we conducted field observations using R/V Hakuo-Maru affiliated with the FMS-KU to measure SSS by casting multiple water quality sensors (AAQ1183; JFE Advantec Co., Ltd., Nishinomiya) at 10 stations around the head of the bay. Using multiple water quality sensors, we obtained the in situ salinity data for surface water sampled with a bucket and sea water averaged over depths of 1–2 m observed by casting. The data were used for cross-checks.

At all observation stations, the surface water (~ 0.5 m) in the bay was sampled to measure the absorbance spectrum of CDOM. Here, we denote as $a_y(\lambda)$ to discriminate satellite-derived $a_{\text{CDOM}}(\lambda)$, which was used as sea truth data. The water samples obtained using a plastic bucket were stored in glass bottles onboard the research vessels and immediately filtered through Whatman GF/F 0.45- μm glass fiber filters to

remove most of the particulate matter. Each sample was filtered again through a 0.2- μm Nucleopore membrane filter to remove fine particles. The absorbance spectrum of each filtrate was scanned over the wavelength range of 300–800 nm to calculate $a_y(\lambda)$ values based on absorbance at 443 nm, $a_y(443)$ with Milli-Q water used for reference, measured by a spectrophotometer (U2900; Hitachi High-Tech Science, Tokyo, Japan) with a 10-cm-long circular quartz cylindrical cell (see Mueller et al. 2003). These observational data were used to derive the SSS– $a_y(443)$ relationship and to validate the satellite-derived absorption coefficient of CDOM, $a_{\text{CDOM}}(400)$ data after removal of error values. For validation, we compared in situ $a_y(443)$ with the satellite-derived $a_{\text{CDOM}}(400)$ because the in situ $a_y(443)$ data were highly correlated with the in situ $a_y(440)$ with $R^2 = 0.99$. In this study, the satellite-derived $a_{\text{CDOM}}(400)$ is referred to as a_{CDOM} for descriptive purposes.

2.2.3 Hourly in situ salinity data

Using the Observing System for Aquatic Quality at Automated Stations in the Osaka Bay (OSAQAS), real-time, in situ salinity observations have been conducted by the MLIT since April 2010. The salinity data were downloaded from the MLIT website (<http://222.158.204.199/obweb/index.aspx>), with an analysis period corresponding to the span of GOCI data, to allow comparison of in situ salinity data with satellite-derived SSS data. OSAQAS consists of observational towers and buoys at 12 stations throughout the bay (Fig. 1), and continuously collects meteorological, oceanographic, and water quality data. The water quality sensors, which travel on a rise and fall system mounted on the tower can observe salinity hourly, averaged over depths of 1–2 m. This observational layer was selected to avoid the surface salinity decrease induced by precipitation, and the layer falls within the plume because the plume bottom is at ~ 2 m in Osaka Bay (Fujiwara et al. 1994a; Hayashi and Yanagi 2008). Due to the potential for biofouling of in-water instrumentation, the sensors were switched out at quarterly intervals.

2.2.4 Hydrometeorological data

Precipitation data in the Yodo River watershed observations from the Automated Meteorological Data Acquisition System (AMeDAS; Fig. 1) were obtained using the Japan Meteorological Agency website (<http://www.data.jma.go.jp/gmd/risk/obsdl>). Time series of daily river runoff from the Yodo River (Takahama station) were obtained from the water information system database (<http://163.49.30.82>) operated by the MLIT. Sites of hydrometeorological observations are shown in Fig. 1. These data were used for analysis of the relationship between river discharge (rainfall) and plumes

Table 1 Dates of observations conducted aboard the R/V Osaka (Marine Fisheries Research Center, Research Institute of Environment, Agriculture and Fisheries, Osaka Prefectural Government; MFRC-OPG) and the R/V Hakuo-Maru (Faculty of Maritime Sciences, Kobe University; FMS-KU)

Year	MFRC-OPG	FMS-KU
2015	August 3–4	August 4
	October 5–6	
	November 2 and 4	
2016	February 1 and 3	November 10
	May 9 and 12	

around a typhoon. The runoff and AMeDAS data covered the analytical period.

2.3 Methodology of calibrated, satellite-derived SSS

A seven-step procedure was used to produce the satellite-derived SSS dataset calibrated by real-time in situ data, as follows (Fig. 2). (1) A tight in situ SSS– $a_y(443)$ relationship was revealed in several field surveys, covering all seasons. (2) An accurate formula to retrieve satellite-derived a_{CDOM} was derived using in situ $a_y(443)$ data collected in the field surveys. (3) A robust relationship between in situ SSS and satellite-derived a_{CDOM} data was developed over a wide salinity range in Osaka Bay. (4) Hourly SSS was estimated from satellite-derived a_{CDOM} using the empirical relationship obtained for the in situ SSS and a_{CDOM} , which is called the “initial estimation”. (5) Estimated SSS was compared to the hourly in situ SSS observed by the real-time monitoring system (OSAQAS); the difference between in situ and satellite-derived SSS, called offset, was obtained. (6) The offset was applied to the satellite-derived SSS map at each grid using Gaussian inter-/extrapolation (Nakada and Isoda 2000). (7) Finally, the calibrated, satellite-derived SSS (GOCI–SSS) map was produced and validated against an independent in situ dataset collected by the OSAQAS.

2.4 Validation of satellite-retrieved sea surface salinity

Three stations (W4, E4, and E5, Fig. 1) that were expected to represent inner-bay salinities in outer plume areas were selected for calibration of the satellite-derived SSS data. In addition, in situ salinity observations from two stations located at the bay head (W2 and E2) were used to validate the satellite-derived SSS, after removal of error data. To match up coincident satellite-derived and in situ data, satellite data acquired within 2.5 km of the stations were averaged to avoid missing data due to cloud cover directly overlying the stations. The horizontal scale of 2.5 km represents the distance that the water mass can move in approximately 1 h with a speed 0.7 m/s, which is a typical tidal advection speed, and indicates the possible time lag of the observation timing between GOCI and in situ observation. We compared data from calibrated, satellite-derived SSS and contemporaneous observations of in situ salinity in the surface layer during the analysis period. The accuracy and precision of the satellite products were quantitatively described using the metrics of bias, root mean square error (RMSE), and determination coefficient following previous studies (e.g., Sasaki et al. 2008).

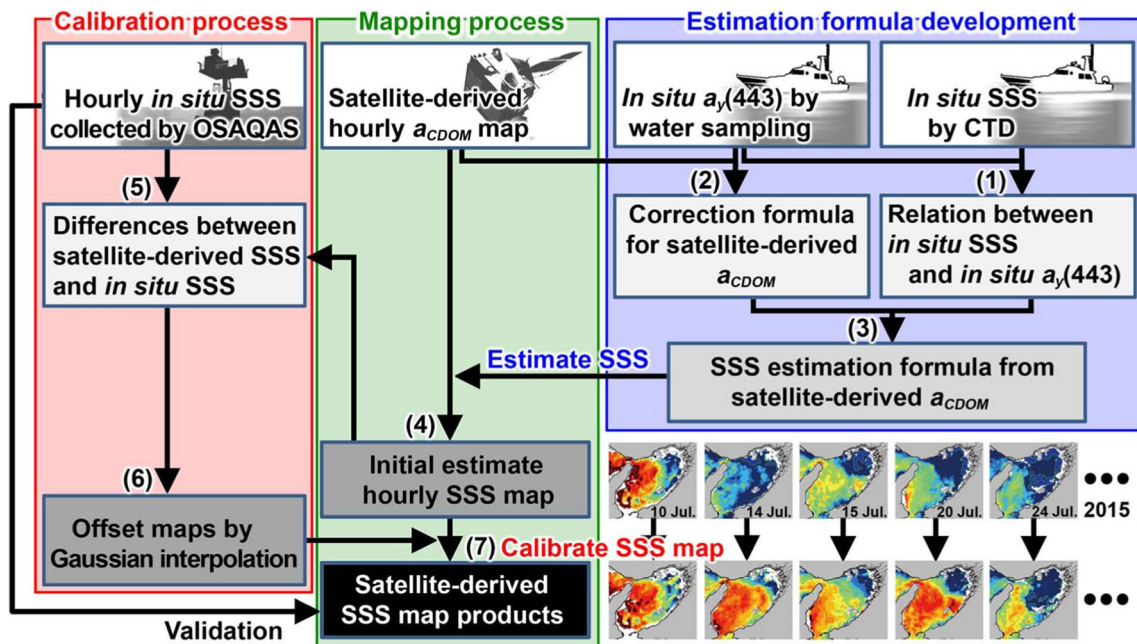


Fig. 2 Flowchart for obtaining initial estimates and calibrated sea surface salinity values from the combined dataset of ocean color satellite, automated observing system (OSAQAS), and hydrographic observations. *Numbers* indicate the process sequence as explained in Sect. 2.3

2.5 Offset maps to calibrate initial estimation of sea surface salinity

The offset maps were produced by objective analysis using Gaussian inter-/extrapolation based on the difference in the hourly matchup data between the in situ and satellite-derived SSS, to improve the estimation accuracy of the initial estimated SSS maps. The matchup data of the satellite-derived SSS were derived at three representative observational stations (W4, E4, and E5) of OSAQAS (Fig. 1) in the same manner as for the validation. The differences derived by the matchup data were interpolated to each grid point with the same horizontal resolution of the SSS maps (500 m) in both zonal and meridional directions using a Gaussian function filter. Its e-folding horizontal scale (influence of the Gaussian radius) is $r_G = 20$ km, which is nearly equal to the average distance (21.6 km) between the three stations (W4, E4, and E5). We analyzed the dependency of the number of stations and e-folding scale on the offset maps, and found that they hardly influence the offset maps, except in the period after a flood (see A1 section in Supplementary Appendix).

2.6 Definition of plume boundaries

To quantify the areas and widths of river plumes, we calculated the effective boundary of the plume (Garvine

1999), defined as the isopleth where the salinity anomaly $s = 0.05$. The SSS map can be converted into a salinity anomaly $s = (S_a - S)/(S_a - S_i)$, where S_a (ambient salinity) and S_i (inlet salinity) represent saline water similar to open-ocean water and the low-salinity water typical of an estuarine source in the bay, respectively. S_a and S_i were calculated using the area-averaged salinity over the bay region ($34.3 < \text{latitude} < 34.8$ and $134.9 < \text{longitude} < 135.5$) and the estuarine region ($34.6 < \text{latitude} < 34.8$ and $135.3 < \text{longitude} < 135.5$), respectively.

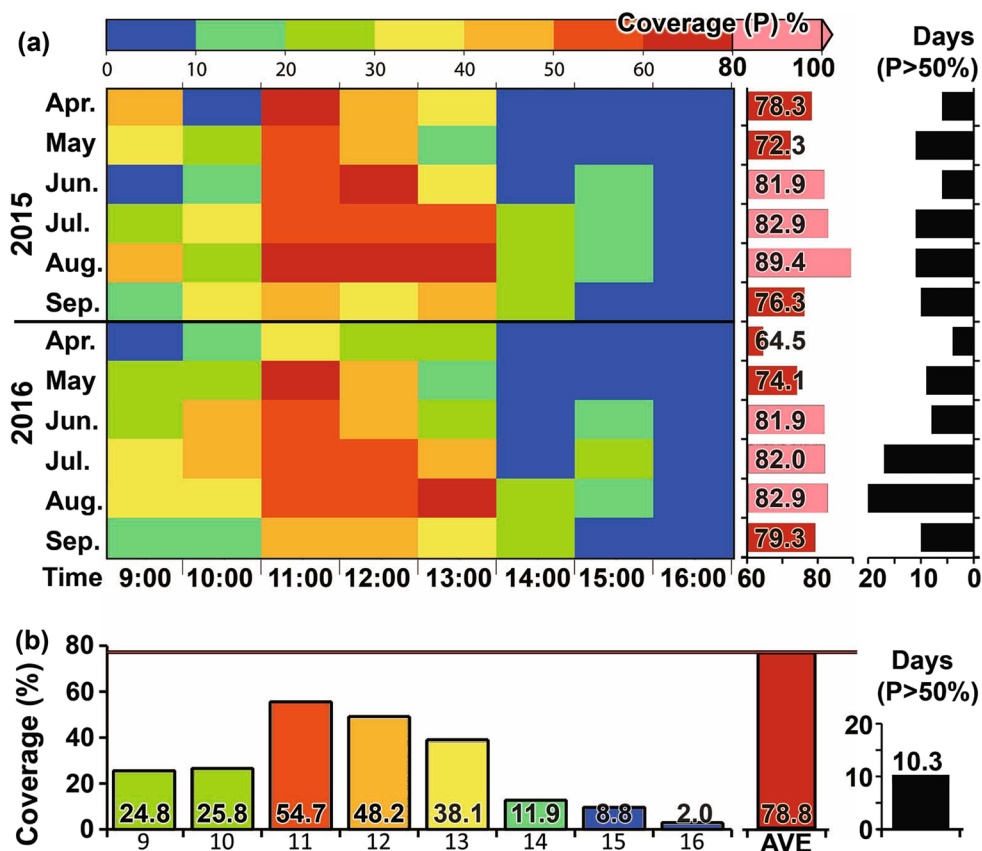
The inlet Rossby radius can be calculated as $r_i = \sqrt{g'\delta}/f$ (Garvine 1999), where $g' = 0.05$ (m s^{-2}) is the reduced gravity, $\delta = 10$ (m) is the water depth in the Yodo River estuary, and f is the Coriolis parameter at a latitude of 34.7°N . These parameters were used for comparison with the width of the river plumes.

3 Results

3.1 Estimation of sea surface salinity using satellite-derived a_{CDOM}

The monthly mean coverage of hourly satellite-derived a_{CDOM} data (left panel in Fig. 3a) indicates that the coverage was relatively high from 11:00 to 13:00, at up to 80%,

Fig. 3 **a** Monthly mean coverages over the analytic area in each hour of ocean color satellite observation during the analytic period from April to September of 2015 and 2016 (left panel). The right panel shows monthly mean values of total daily coverage and total days per month with coverage of more than half of the analytic area ($p > 50\%$). **b** Coverage averaged over the analytic period in hourly (left), and average days with $p > 50\%$ (right)



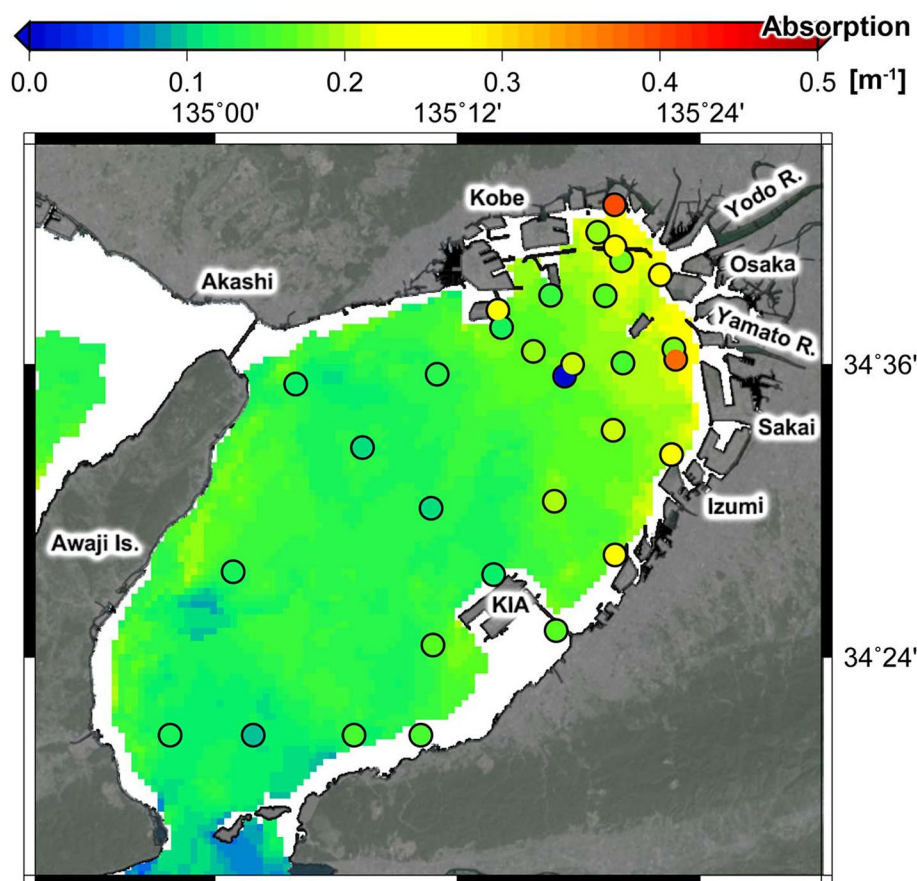
but was generally low from 14:00 to 16:00 (up to 30%) during the analytical period. Based on 8 hourly observations, the total daily coverage (right panel) always exceeded 70% except in April 2016, and was highest in August of both years. The left panel in Fig. 3b indicates that the total mean coverage for each hour was below 55% (highest at 11:00). Meanwhile, the total daily coverage (right panel) improved to nearly 80% upon integration of the hourly data. There were 10 or more days per month with coverage $p > 50\%$ (Fig. 3a) in summer (July–September), but less in spring (April–June). The average number of days per month was 10.3, indicating that one third of the data collected in a month were available for our analysis. The observational errors attributed to the solar zenith angle have less influence on our study because the data coverage at 9:00 and 16:00 was lower than 25%, although the present GDPS does not remove the errors sufficiently.

As an example of a_{CDOM} observations, Fig. 4 shows a comparison between satellite-derived a_{CDOM} and in situ $a_y(443)$. Most satellite-derived a_{CDOM} values were lower than 0.4 m^{-1} . The a_{CDOM} map indicates higher values in the northeastern part of the bay (approximately 0.25 m^{-1}), especially in regions along the coast of the bay head. The a_{CDOM} values decreased southwestward down to 0.05 m^{-1} . The distribution of $a_y(443)$ is similar to that of a_{CDOM} , indicating

$a_y(443)$ data roughly covaried with a_{CDOM} . However, the a_{CDOM} values were lower than $a_y(443)$ at two nearshore stations, which had $a_y(443)$ values of approximately 0.4 m^{-1} , indicating substantial underestimation of a_{CDOM} . This underestimation may be attributed to differences in observational date and time, because the fluctuation of CDOM can be greater around nearshore regions. Satellite-derived a_{CDOM} could not be obtained for the dates when field sampling was conducted (3 and 4 August) due to cloud cover. Thus, for the validation process, we used daily-averaged satellite data for 5 August (5–6 h).

The scatterplot of satellite-derived a_{CDOM} and in situ $a_y(443)$; Fig. 5a) using available matchup data from 5 August and 4 November shows a strong, significant correlation, with a determination coefficient of $R^2 = 0.75$ ($n = 60$, $p = 3.5 \times 10^{-19}$). Regression analysis generated a good fit to the data, indicating the satellite-derived a_{CDOM} can be quantitatively verified for our analysis. Most of the corrected a_{CDOM} data (not shown) fell near the 1:1 line (RMSE 0.034). Strong, significant correlations were also found between the observed SSS and in situ $a_y(443)$, with a high determination coefficient of $R^2 = 0.85$ ($n = 135$, $p = 1.5 \times 10^{-50}$) in the scatterplot (Fig. 5b) containing multiple months, indicating that seasonal dependency was minor (see section A2 in Supplementary Appendix). As a result of these regression

Fig. 4 Geographic distribution of satellite-derived a_{CDOM} and in situ (observed) $a_y(443; \text{m}^{-1})$ on 5 August and 3–4 August 2015, respectively



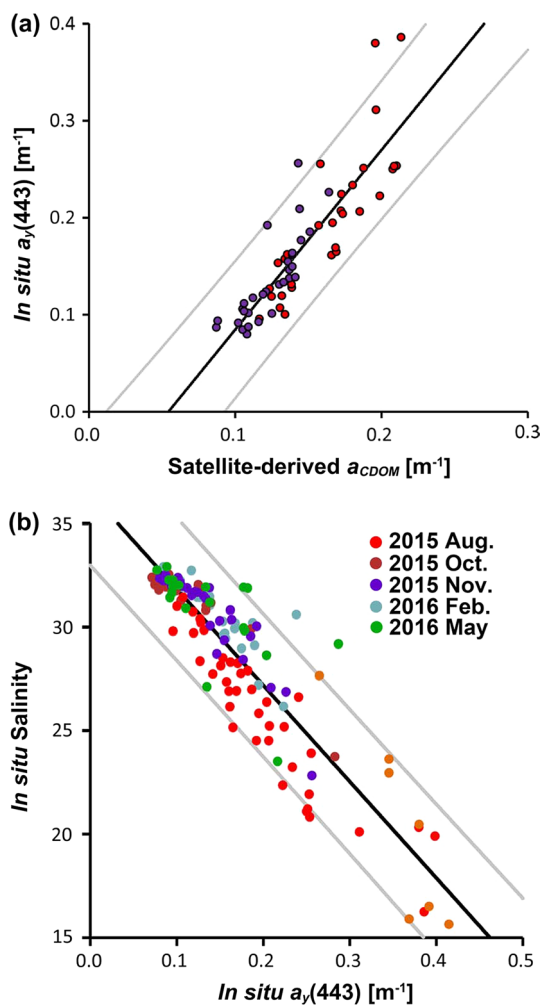


Fig. 5 **a** Scatter plot comparing satellite-derived a_{CDOM} and in situ (observed) $a_y(443; m^{-1})$ data in match-up periods from 3 to 5 August and 2–4 November 2015. **b** Scatter plot showing in situ $a_y(443; m^{-1})$ and in situ sea surface salinity in summer (August 2015), fall (October and November 2015), winter (February 2016), and spring (May 2016). *Gray lines* represent the 95% prediction interval

analyses, the following empirical formula was used to estimate satellite-derived SSS from satellite-derived a_{CDOM} :

$$\text{Initial estimate SSS} = -105.78a_{CDOM} + 44.06. \tag{1}$$

Most estimates of SSS in the matched data followed the 1:1 line (Fig. 6), with moderate accuracy (RMSE 1.578, bias 0.000, $R^2 = 0.85$, $n = 135$, $p = 3.1 \times 10^{-25}$). The RMSE is sufficient to resolve the wide range of salinity (20–34) in Osaka Bay.

3.2 Accuracy of satellite-derived sea surface salinity

Figure 7 shows two examples of the initial estimated and calibrated SSS maps from 14 July and 18 August. An

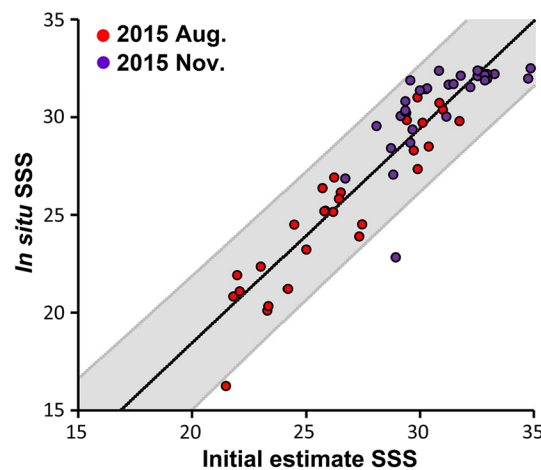


Fig. 6 Comparison of satellite-derived and observed (in situ) sea surface salinity. *Gray lines* and areas represent the 95% prediction interval

unrealistically low-salinity distribution was visible throughout the bay on 14 July (Fig. 7a). These excessively low-salinity values were successfully calibrated using hourly salinity data collected by the automatic monitoring system (OSAQAS), as shown by Fig. 7b. The SSS map on 18 August (Fig. 7c) shows high-salinity water around the Akashi Strait, which was modified by the low-salinity water distribution (Fig. 7d). These errors may be wholly or partially attributed to insufficient atmospheric correction in the GDPS algorithm or estimation errors of a_{CDOM} , as discussed in Sect. 5. These results indicate that utilization of automated water quality monitoring data can contribute to whole or partial modification of satellite-derived SSS maps.

Next, we will show the validity of the calibrated SSS data, as verified using in situ SSS data derived from the OSAQAS. In situ SSS data were selected to match the available satellite-derived data at W4, E4, and E5 that were used for calibration (Fig. 2). The in situ SSS data at stations W2 and E2 in the nearshore area of the bay head were independent of the calibration data and used to validate the satellite-derived SSS. To ensure the data are sufficient for comparison, quality control was conducted on the estimated SSS data to meet the conditions of sufficient satellite data coverage over Osaka Bay ($p > 15\%$) without extremely low or high $a_y(443)$ values, which led to the exclusion of data derived at hours 15:00 and 16:00 and on 27 April, 2 May, 29 June, and 23–28 August.

Figure 8a shows a scatterplot of the initial SSS estimates and in situ SSS data collected at the station, which were used for calibration. The determination coefficient was low ($R^2 = 0.03$, $n = 645$, $p = 4.3 \times 10^{-5}$) although the correlation was significant, suggesting that the accuracy of the initial estimate is insufficient for analysis (RMSE 5.1, bias 17.9). On the other hand, a strong, significant

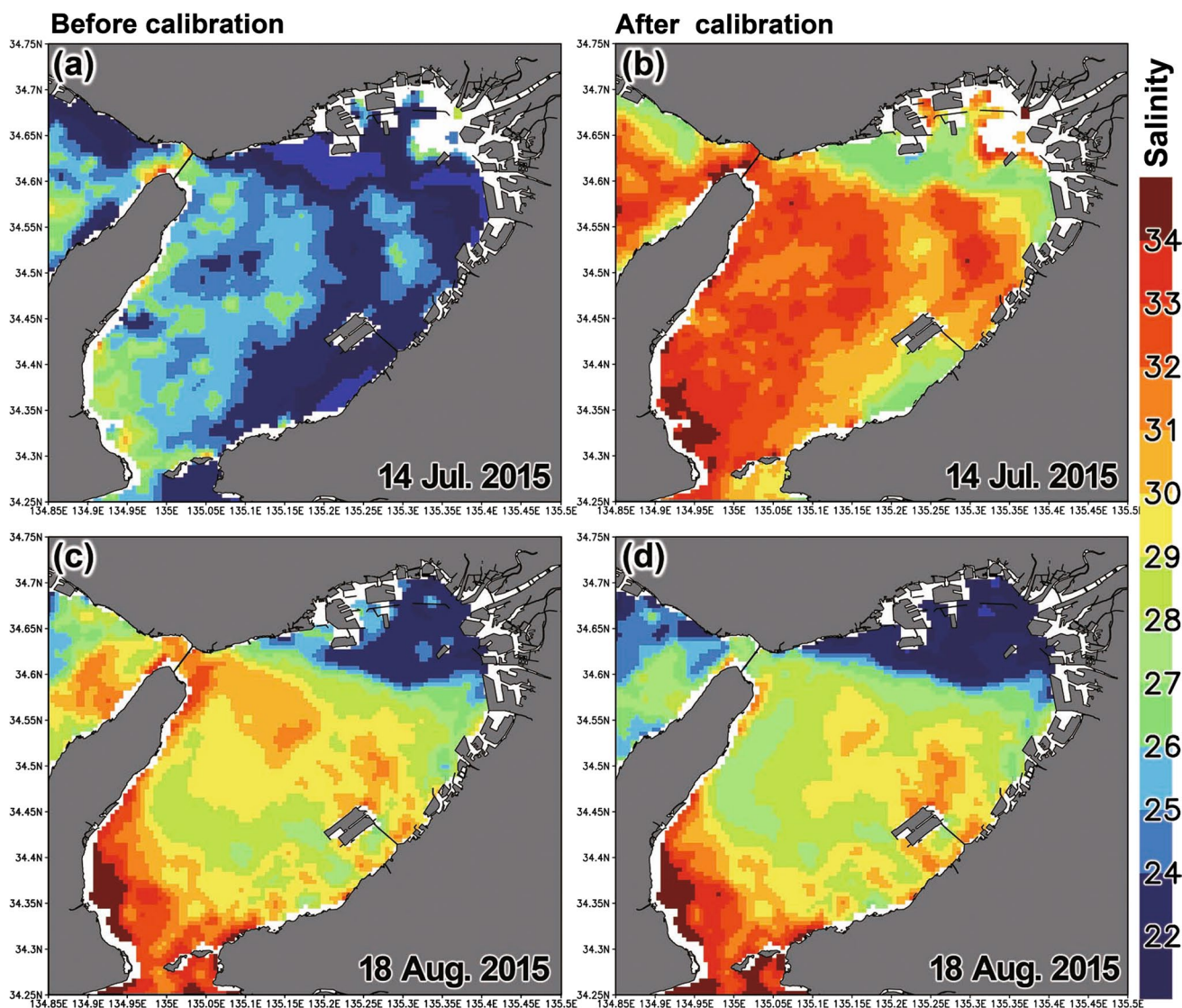


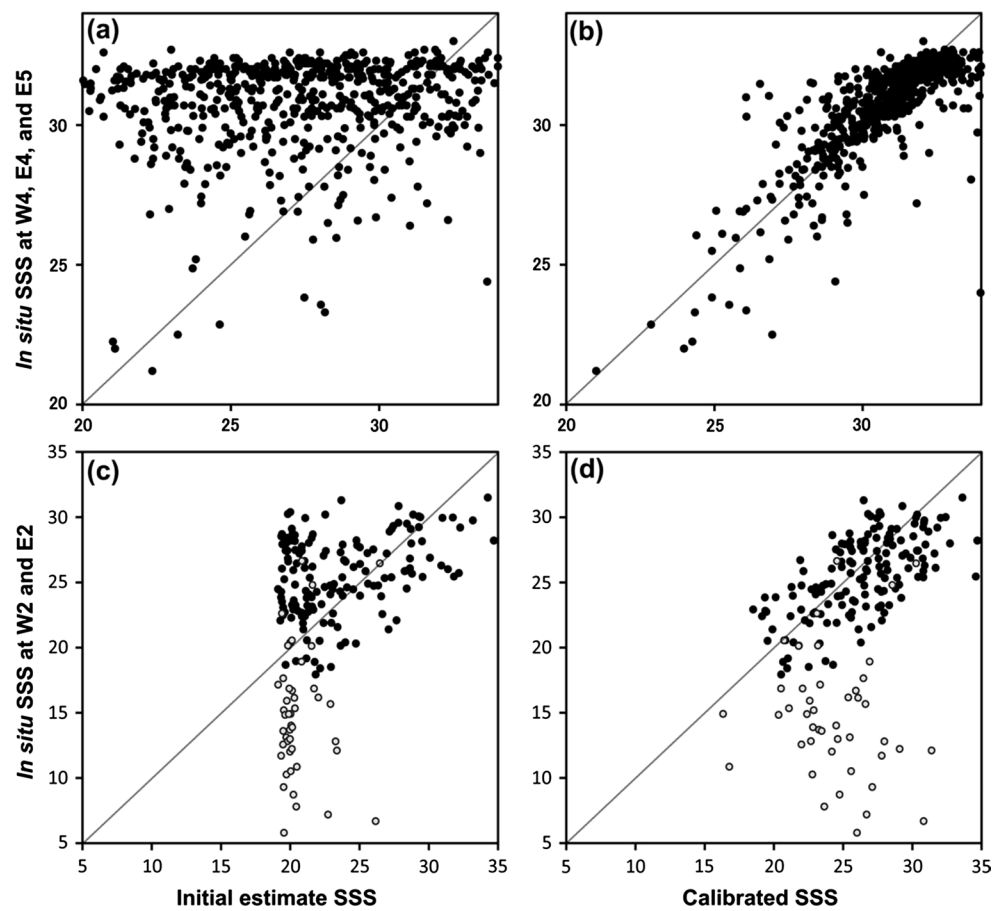
Fig. 7 Maps of satellite-derived sea surface salinity from the initial estimate before calibration (a, c) and final estimate after calibration (b, d) on 14 July and 18 August 2015

correlation ($R^2 = 0.57$, $n = 645$, $p = 2.0 \times 10^{-120}$) was found between the calibrated satellite-derived SSS and in situ SSS data (Fig. 8b), with data falling close to the 1:1 line (RMSE 1.5), indicating that most of the initial SSS estimates were successfully calibrated. The scatter plot of the initial estimates of SSS and in situ SSS data observed in the bay head (Fig. 8c) also exhibited insufficient accuracy ($R^2 = 0.10$, $n = 152$, $p = 6.9 \times 10^{-5}$, RMSE 4.6). The black dots in Fig. 8d indicate an improvement of accuracy ($R^2 = 0.40$, $n = 152$, $p = 1.3 \times 10^{-18}$) for more than half of the calibrated data (66%), which fell close to the 1:1 line (RMSE 2.9). However, the estimated SSS on 15–31 July (open circles) failed to be calibrated, because large runoff events from the Yodo River (as explained in detail below) can form low-salinity water in the nearshore area of the

bay head beyond the lower limit (approximately 20) of the salinity estimation model (Fig. 6).

Thus, the accuracy of satellite-derived SSS estimation in the bay was also significantly improved by using real-time, in situ SSS data derived from an automated observation system (OSAQAS). As a result, the estimation error (RMSE) in the bay was decreased by 71% from the initial estimation, and the determination coefficient increased approximately 20-fold. For SSS data at stations in the nearshore area of the bay head, the estimation error (RMSE) was decreased by 37% and the determination coefficient quadrupled. The accuracy of calibrated SSS data (final estimation) is acceptable for analysis of the river plume because the plume is characterized by a wide horizontal gradient of SSS (range 20–34).

Fig. 8 Comparison of initial estimates (*left panels*) and calibrated values (*right panels*) of sea surface salinity. In situ salinity, used in the *upper and lower panels*, was observed at the western offshore stations (W4, E4, and E5: *red rectangles* in Fig. 1) of OSAQAS and at the stations in the bay head (W2 and E2: *blue rectangles*), respectively. Plots were divided into a group with RMSE < 1.5 (*black dots*) and other data (*open gray circles*)



3.3 Errors in the satellite-derived sea surface salinity

The cumulative error e_i , which the initially estimated SSS maps should retain before calibration, can be described by $e_i = \sqrt{(e_1)^2 + (e_2)^2 + (e_3)^2}$ based on the error propagation rules from procedures (1) to (4), as shown in the flowchart (Fig. 2). Here, e_1 is the error attributed to the in situ $a_y(443)$ estimation from the satellite-derived a_{CDOM} , e_2 is the error of the empirical formula for in situ SSS estimated from the in situ $a_y(443)$, and e_3 is the error produced by processing the initial estimation for the SSS maps. Each error can be referred to as the RMSE based on salinity; we calculated $e_1 = 1.51$ (Fig. 5a) and $e_2 = 1.91$ (Fig. 5b), but e_3 was difficult to calculate because there were multiple causes of error. Here, $e_i = 4.6$ can be derived from the accuracy evaluation of the satellite-derived SSS (Fig. 8a). As a result, we obtained $e_3 = 3.9$ based on the error propagation rules. The contributions of each error to the cumulative error e_i^2 were also calculated as percentages, e_1^2 (10.8%), e_2^2 (17.2%), and e_3^2 (72.0%). The percentages indicate that the empirical formula in Eq. (1) is uniformly applied to the satellite-derived a_{CDOM} maps to be converted into the SSS in space and time, leading to the large error contribution (72%). The calibration

can significantly reduce this error (RMSE or $e_c = 2.9$) in the case of the stations E2 and W2. Here, e_c is the error of the calibrated SSS data. These results indicate the importance of calibration using a time series of in situ SSS data.

4 Analysis of river plumes using SSS maps

4.1 Monthly-averaged SSS

Figure 9 shows monthly-averaged SSS maps (colors) with the effective boundaries of the plume indicated (solid lines) in Osaka Bay from August in 2015 to September 2016. The seasonal SSS patterns indicate that the river plume located in the bay head area and its salinity decreased from June to August. In this period, the plume area, demarcated by the plume boundary, shows that the plume area gradually extended southwestward from the bay head and its cross-shelf width tapered around the southwestern coast of the bay. These features are largely consistent with the findings of previous reports based on low-resolution SSS maps estimated from in situ observations (e.g., Nakajima 1997), which supports the validity of the satellite-derived SSS.

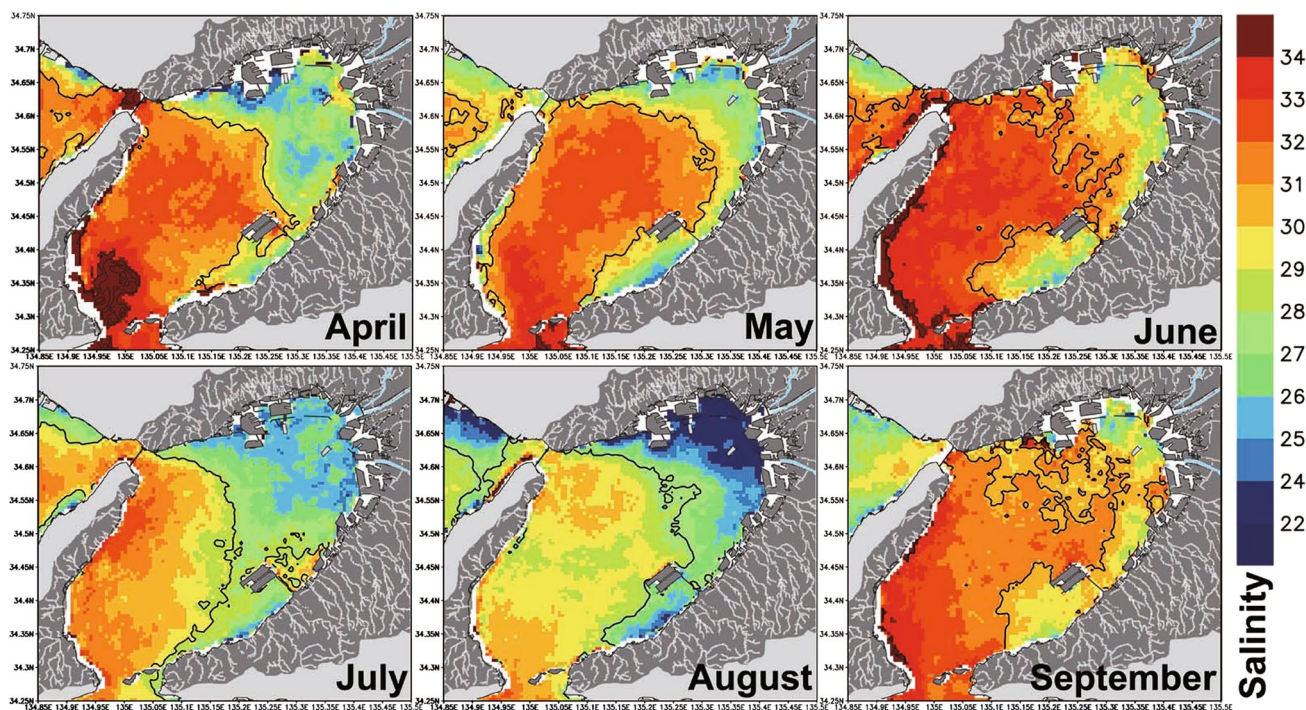


Fig. 9 Maps of monthly mean sea surface salinity collected by GOCI-COMS from April to September of the analysis period. *Solid lines* indicate the effective boundary of the plume. *Pale blue lines* in the watershed indicate river paths

The SSS maps in July (Fig. 9) show the plume distributed along the southwestern coast, suggesting that the plume flowed toward the Pacific Ocean through the eastern portion of Kitan Strait. The typical width of the low-salinity water plume was 6.9 km, comparable to the characteristic scale of the inlet Rossby radius, $r_i = 7.7$ km. These results suggest that the low-salinity water discharged from the river turns left along the coast and forms a growing intrusion known as a type 2 plume (Garvine 2001). Furthermore, the small-scale patches of low-salinity water (< 26) along the southwestern coast around Kansai International Airport (KIA) is visible in the satellite-derived SSS map, implying that the plume may be not only formed by runoff from the Yodo River but also from several small rivers located along the southern coast of the bay.

4.2 River plume induced by typhoon

Figure 10a shows the observed temporal variation of the daily mean Yodo River discharge and total precipitation in its watershed. The large precipitation peak on 17 July indicates heavy rainfall attributed to a category 4 super typhoon, Nangka, leading to large discharge from the Yodo River from 17 to 18 July. Discharge gradually decreased in the post-typhoon period from 19 to 29 July, and was relatively constant at $1000 \text{ m}^3 \text{ s}^{-1}$ until 24 July, then further decreased to approximately $300 \text{ m}^3 \text{ s}^{-1}$ on July 29.

The Hovmöller diagram of SSS observations from OSAQAS (Fig. 10b) displayed temporal variation of low-salinity surface water in response to large runoff events. SSS observed in the pre-typhoon period exhibited a low salinity of 14–26 around the estuary (W2, W1, E1, and E2) and increased to 30 during the typhoon at E1, implying that vertical mixing was enhanced by the strong wind. Then, the salinity decreased due to the large freshwater input on 17 July; low-salinity water appeared again on 18 July, which rapidly extended westward and southward to the Akashi and Kitan Straits along the west and east coasts, respectively.

The SSS distributions differ notably between the pre- and post-typhoon periods (Fig. 11). Comparing the distributions on 15 and 20 July indicated that low-salinity water in the bay head spread southward after the large runoff peak on 18 July, and extended along the southeast coast around KIA. The eastern front of low-salinity water intruded into Akashi Strait. Based on the effective boundary of the plume in the bay head, the area within the plume changed from 360.1 km^2 in the pre-typhoon period to 533.1 km^2 post-typhoon. The post-typhoon plume covered half of Osaka Bay; the change in area associated with the runoff peak was approximately 1.5-fold. Hourly changes in low-salinity water were rarely found, suggesting that estimation errors in the areas attributed to wind-driven or tidal transport of the low-salinity water were negligible in this period.

Fig. 10 **a** Temporal variations in total daily precipitation ($\text{m}^3 \text{s}^{-1}$) estimated from AMeDAS data over the Yodo River watershed and runoff ($\text{m}^3 \text{s}^{-1}$) observed at Takahama (Fig. 1) during the pre-typhoon to post-typhoon period (10–29 July 2015). *Solid lines* indicate days for which satellite data were available. **b** Hovmöller diagrams of hourly nearshore sea surface salinity along the coast of the bay from 10 to 29 July 2015. The ten letter and number combinations (E1–E5 and W1–W5) correspond to the OSAQAS stations (Fig. 1). Stations E1 and W1, as shown on the vertical axis, are located in the estuaries of the Yodo and Yamato Rivers, respectively. *Black rectangles* in the diagram indicate missing data

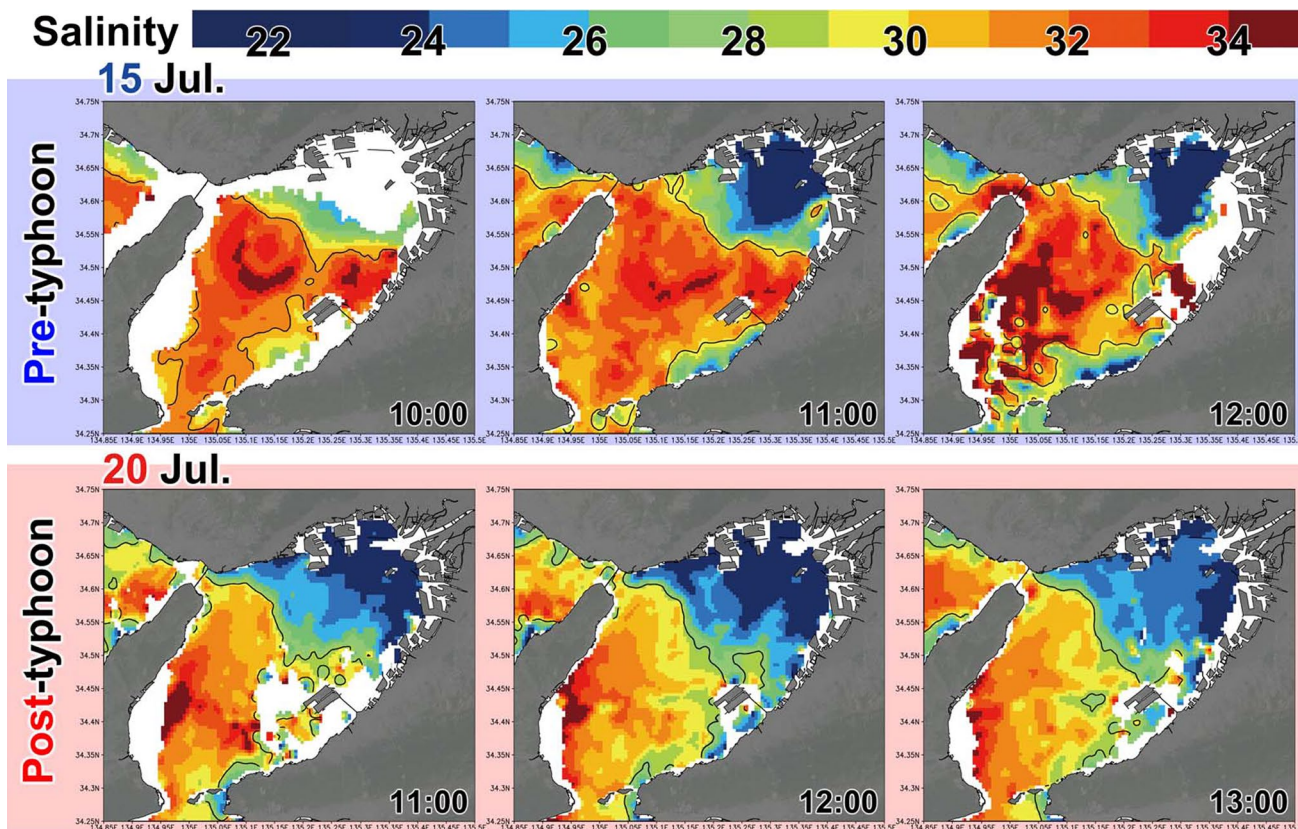
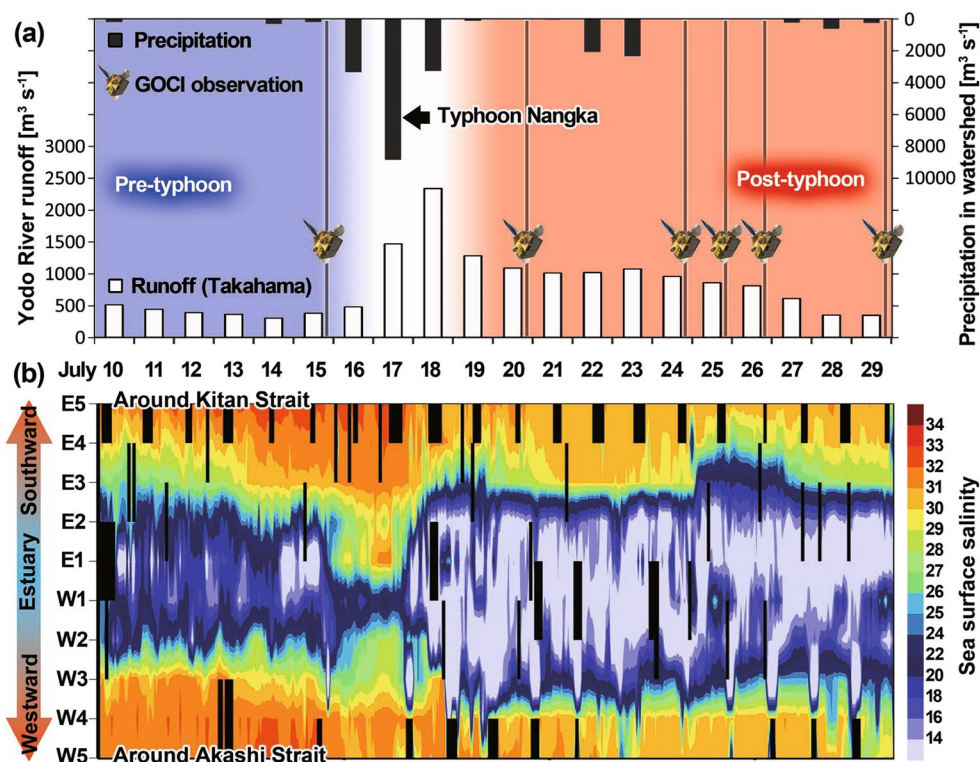


Fig. 11 Hourly maps of sea surface salinity derived from GOCI to COMS in the pre-typhoon (15 July 2015) and post-typhoon (20 July 2015) periods. *Solid lines* indicate the effective boundary of the plume

Fig. 12 **a** Temporal variation of the effective boundary of the plume from 15 to 26 July 2015. **b** Map of sea surface salinity and the effective boundary of the plume (*solid line*) on 29 July 2015

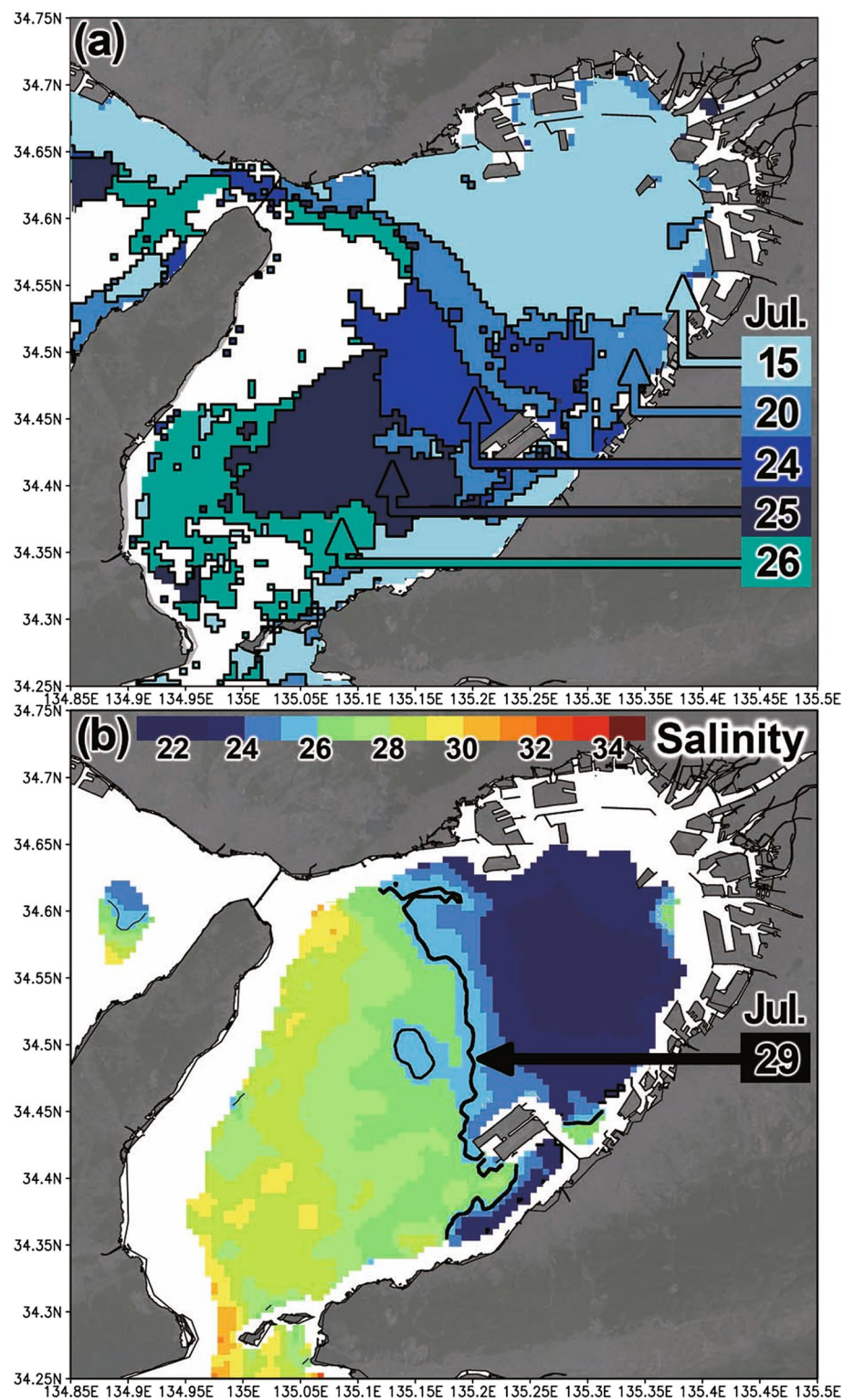


Figure 12a shows the temporal change in the area within the daily-averaged effective boundary of the plume. This figure indicates that low-salinity water migrated southwestward to the bay mouth in the post-typhoon period. The migration speed was approximately 7 km day^{-1} (0.08 m s^{-1}). A jut

in the boundary was visible in the center of the bay on 25 July, and this jut propagated southwestward along the bay axis, leading to an extension of the low-salinity water in the southern part of the bay. Then, the low-salinity water flowed out through Kitan Strait during the period of 26–29 July,

while a large area of low-salinity water (< 26) remained in the eastern portion of the bay on 29 July (Fig. 12b). The area of low-salinity water shrank nearly to its pre-typhoon extent on 31 July, indicating that the duration of the SSS decrease in the bay induced by the large freshwater discharge from the typhoon was approximately 2 weeks.

5 Discussion

This paper presents a methodology to produce and improve high-resolution SSS maps in ROFI based on ocean color observations from a geostationary satellite in conjunction with an automated observing system (OSQAS) to collect time series in situ SSS data. The implementation of a procedure to calibrate SSS could suppress two types of estimation errors. One of these is error in the empirical formula for the SSS– a_{CDOM} relationship, which can be attributed to regional hydrodynamic and biogeochemical processes (Bai et al. 2013). In local coastal waters, an empirical methodology based on the SSS– a_{CDOM} relationship may be regulated by regional and seasonal variations (Bai et al. 2013). For example, marine CDOM sources (autochthonous production of CDOM) can be induced by sediment resuspension associated with atmospheric disturbances (Boss et al. 2001) and by biological effects such as the degradation of coastal phytoplankton and microbial decomposition (Nelson et al. 1998, 2010; Twardowski and Donaghay 2001; Coble et al. 2004; Stedmon and Markager 2005). On the other hand, decreases in CDOM can be induced by microbial consumption (Del Vecchio and Blough 2004) and photochemical bleaching (Chen et al. 2004) of labile and semi-labile DOM (Keller and Hood 2011; Kobayashi et al. 2017). Errors attributable to these processes may affect the SSS map on 18 August (Fig. 7), in which a lower SSS range around the estuary and bay head was estimated before local calibration. However, seasonal and regional variations in the SSS– $a_y(443)$ relationship in Osaka Bay were rarely observed in the field surveys. Another estimation error can be attributed to the atmospheric correction algorithm used for remote sensing reflectance (e.g., He et al. 2012; Wang et al. 2007) and the bio-optical model used to estimate a_{CDOM} (e.g., Lee et al. 2002; Zhu et al. 2011). Errors attributed to these complex processes can propagate and limit the accuracy of satellite-derived a_{CDOM} , leading to unrealistically low SSS, as was seen on 14 July (Fig. 7). This result implies that the increase of land-based aerosols may not be fully accounted for in the atmospheric correction algorithm (Vogel and Brown 2016), leading to overestimation of a_{CDOM} in the bay.

Our results suggest that the observations of SSS time series at appropriate locations in the coastal sea is essential for practical application of satellite-derived SSS to the coastal sea, although efforts should be undertaken in the

future to improve the satellite-derived a_{CDOM} algorithm in coastal waters. In Japanese coastal seas, automated systems to observe salinity, such as OSQAS, are already operating in larger bays (e.g., Ise Bay, Tokyo Bay, and Funka Bay), showing that our approach can be applied immediately in those coastal areas. Note that the application of our methodology to other coastal seas is possible under the following three assumptions: (1) the spatiotemporal variation in the SSS is mainly dominated by freshwater supply via the riverine discharge and its mixing with coastal seawater, (2) the terrestrial CDOM in the coastal seas greatly exceed the marine CDOM, and (3) the horizontal pattern in satellite-derived a_{CDOM} maps may be qualitative because the GOCI observations could retain an unknown large-scale bias.

Typhoons (tropical storms) are the most energetic extreme weather events affecting the environment and ecosystem in estuarine and coastal areas (Herbeck et al. 2011). However, the dynamics of river plumes formed by large runoff events caused by typhoon strikes remain poorly understood. These events have been studied primarily using numerical modeling (e.g., Liu et al. 2002) due to the absence of observations collected at high temporal frequency and horizontal density. Our results show the detailed dynamics of the river plume influenced by extreme runoff during the typhoon period in Osaka Bay. The low-salinity water of the plume tends to be distributed from Kobe City to Akashi Strait along the northern coast (Fig. 11), supporting the westward advection of the plume when discharge from the Yodo River increases markedly due to flood events (Fujiwara et al. 1994a). Then, the plume migrated southwestward along the east coast toward the bay mouth (Fig. 12), with a migration speed of 0.08 m/s, comparable to the flow speed of the Okino-se circulation (Fujiwara et al. 1994b) but smaller than the propagation speed of an internal Kelvin wave, $C_i = \sqrt{g'\delta} = 0.7 \text{ m s}^{-1}$. Therefore, the Okino-se circulation may play an important role in transporting the river plume, high in nutrients and turbidity, to outer Osaka Bay through the Kitan Strait within 2 weeks after a typhoon. Thus, SSS data with high spatiotemporal resolution can be used to observe the marked increase in low-salinity water induced by typhoons. Additional studies may provide further statistical analysis of the detailed plume dynamics when satellite-derived SSS data surrounding typhoon events are accumulated in the future.

6 Conclusions

This paper proposed a novel methodology to produce spatiotemporally high-resolution ($\sim 500 \text{ m}$) SSS maps for analysis of the river plume and coastal oceans at a local scale ($\sim 10^3 \text{ km}^3$), based on hourly ocean color products derived from geostationary satellite observations. The estimation accuracy of the satellite-derived SSS data was improved by

utilization of time series in situ SSS data collected by an automated observation system. As a result, estimation error of satellite-derived SSS substantially decreased (37–71%) within a wide range of SSS (20–34). Dynamics of the river plume induced by typhoon-generated runoff was first comprehensively investigated using time series in situ SSS and hydrological data and a satellite-derived SSS (GOCI–SSS) map. After calculating the salinity anomaly based on the satellite-derived SSS map, the effective boundary of the plume could be used to identify quantitatively the area and width of river plumes. The plume area covered half of the bay during the post-typhoon period, and was approximately 1.5 times as large as in the pre-typhoon period, leading to a decrease of the SSS in the bay during the 2 weeks following the storm. The plume in the bay head intruded into the Akashi Strait after the large runoff event, while the plume also extended southward along the southeast coast to the bay mouth, where it flowed out through Kitan Strait. Our approach provides a practical method of analyzing the dynamics of low-salinity riverine plumes in coastal oceans, which may lead to the development of improved coastal ocean models for operational oceanography, ocean forecasting (Urakawa et al. 2015), and disaster reduction (Nakada et al. 2016).

Acknowledgements This work was supported primarily by the Fund of the Japan Society for the Promotion of Science (nos. 26887025, 16K13882) and the Kurita Water and Environment Foundation (KWEF), Japan, and was carried out in part by the Collaborative Research Program of Research Institute for Applied Mechanics, Kyushu University and the joint research program of the Institute for Space-Earth Environmental Research (ISEE), Nagoya University. The authors sincerely thank Dr. T. Yanagi in the EMECS center and Prof. M. Hayashi at Kobe University for their comments. Part of this work used the computational resources of the supercomputer ACCMS, Kyoto University. We deeply appreciate the constructive comments from two anonymous reviewers and editor, Prof. T. Hirawake.

References

- Amin R, Gould R, Ladner S, Shulman I, Jolliff J, Sakalaukus P, Lawson A, Martinolich P, Arnone R (2013) Inter-sensor comparison of satellite ocean color products from GOCI and MODIS. In: AMS Proceedings, p 5
- Bai Y, Pan D, Cai W, He X, Wang D, Tao B, Zhu Q (2013) Remote sensing of salinity from satellite-derived CDOM in the Changjiang River dominated East China Sea. *J Geophys Res Oceans* 118:227–243. <https://doi.org/10.1029/2012JC008467>
- Bai Y, He X, Pan D, Chen CTA, Kang Y, Chen X, Cai WJ (2014) Summertime Changjiang River plume variation during 1998–2010. *J Geophys Res Oceans* 119:6238–6257. <https://doi.org/10.1002/2014JC009866>
- Binding CE, Bowers DG (2003) Measuring the salinity of the Clyde Sea from remotely sensed ocean colour. *Estuar Coast Shelf Sci* 57:605–611. [https://doi.org/10.1016/S0272-7714\(02\)00399-2](https://doi.org/10.1016/S0272-7714(02)00399-2)
- Boss E, Pegau WS, Zaneveld JRV, Barnard AH (2001) Spatial and temporal variability of absorption by dissolved material at a continental shelf. *J Geophys Res* 106:9499–9507
- Bowers DG, Brett HL (2008) The relationship between CDOM and salinity in estuaries: an analytical and graphical solution. *J Mar Syst* 73(1–2):1–7
- Chen Z, Li Y, Pan J (2004) Distributions of colored dissolved organic matter and dissolved organic carbon in the Pearl River Estuary, China. *Cont Shelf Res* 24:1845–1856
- Coble P, Hu C, Gould RW Jr, Chang G, Wood AM (2004) Colored dissolved organic matter in the coastal ocean: an optical tool for coastal zone environmental assessment and management. *Oceanography* 17(2):50–59
- Del Castillo CE, Miller RL (2008) On the use of ocean color remote sensing to measure the transport of dissolved organic carbon by the Mississippi River Plume. *Remote Sens Environ* 112:836–844. <https://doi.org/10.1016/j.rse.2007.06.015>
- Del Castillo CE, Coble PG, Morell JM, Lopez JM, Corredor JE (1999) Analysis of the optical properties of the Orinoco River plume by absorption and fluorescence spectroscopy. *Mar Chem* 66(1–2):35–51
- Del Vecchio R, Blough Neil V (2004) Spatial and seasonal distribution of chromophoric dissolved organic matter and dissolved organic carbon in the Middle Atlantic Bight. *Mar Chem* 89:169–187
- Del Vecchio R, Subramaniam A (2004) Influence of the Amazon River on the surface optical properties of the western tropical North Atlantic Ocean. *J Geophys Res* 109:C11001. <https://doi.org/10.1029/2004JC002503>
- Fichot CG, Lohrenz SE, Benner R (2014) Pulsed, cross-shelf export of terrigenous dissolved organic carbon to the Gulf of Mexico. *J Geophys Res Oceans* 119(2):1176–1194. <https://doi.org/10.1002/2013JC009424>
- Font J, Camps A, Borges A, Martín-Neira M, Boutin J, Reul N, Kerr YH, Hahne A, Mecklenburg S (2010) SMOS: the challenging sea surface salinity measurement from space. *Proc IEEE* 98(5):649–665. <https://doi.org/10.1109/JPROC.2009.2033096>
- Fujiwara T, Sawada Y, Nakatsuji K, Kuramoto S (1994a) Water exchange time and flow characteristics of the upper water in the eastern Osaka Bay—anticyclonic circulation in the head of the estuary. *Bull Coast Oceanogr* 31(2):227–238 (in Japanese with English abstract)
- Fujiwara T, Nakata H, Nakatsuji K (1994b) Tidal-jet and vortex-pair driving of the residual circulation in a tidal estuary. *Cont Shelf Res* 14(9):1025–1038
- Garvine RW (1999) Penetration of buoyant coastal discharge onto the continental shelf: a numerical model experiment. *J Phys Oceanogr* 29:1892–1909
- Garvine RW (2001) The impact of model configuration in studies of buoyant coastal discharge. *J Mar Res* 59:193–225
- Geiger EF, Grossi MD, Trembanis AC, Kohut JT, Oliver MJ (2013) Satellite-derived coastal ocean and estuarine salinity in the Mid-Atlantic. *Cont Shelf Res* 63:S235–S242. <https://doi.org/10.1016/j.csr.2011.12.001>
- Hansell DA (2013) Recalcitrant dissolved organic carbon fractions. *Annu Rev Mar Sci* 5:421–445. <https://doi.org/10.1146/annurev-marine-120710-100757>
- Hayashi M, Yanagi T (2008) Analysis of change of red tide species in Yodo River estuary by the numerical ecosystem model. *Mar Pollut Bull* 57:103–107. <https://doi.org/10.1016/j.marpolbul.2008.04.015>
- He X, Bai Y, Pan D, Tang J, Wang D (2012) Atmospheric correction of satellite ocean color imagery using the ultraviolet wavelength for highly turbid waters. *Opt Express* 20(18):20754–20770
- Herbeck LS, Unger D, Krummea U, Liu SM, Jennerjahn TC (2011) Typhoon-induced precipitation impact on nutrient and suspended matter dynamics of a tropical estuary affected by human activities in Hainan, China. *Estuar Coast Shelf Sci* 93:375–388
- Hoshika A, Tanimoto T, Mishima Y (1994) Sedimentation processes of particulate matter in the Osaka Bay. *Oceanogr Jpn* 3(6):419–425

- Hu C, Montgomery ET, Schmitt RW, Muller-Karger FE (2004) The dispersal of the Amazon and Orinoco River water in the tropical Atlantic and Caribbean Sea: observation from space and S-PALACE floats. *Deep-Sea Res II* 51:1151–1171. <https://doi.org/10.1016/j.dsr2.2004.04.001>
- Kawahara M, Uye S, Ohtsu K, Iizumi H (2006) Unusual population explosion of the giant jellyfish *Nemopilema nomurai* (Scyphozoa: Rhizostomeae) in East Asian waters. *Mar Ecol Prog Ser* 307:161–173
- Keller DP, Hood RR (2011) Modeling the seasonal autochthonous sources of dissolved organic carbon and nitrogen in the upper Chesapeake Bay. *Ecol Model* 222:1139–1162
- Kerr YH, Waldteufel P, Wigneron J, Delwart S, Cabot F, Boutin J, Escorihuela MJ, Font J, Reul N, Gruhier C (2010) The SMOS mission: new tool for monitoring key elements of the global water cycle. *Proc IEEE* 98(5):666–687. <https://doi.org/10.1109/JPRO.2010.2043032>
- Kobayashi S, Matsumura Y, Kawamura K, Nakajima M, Yamamoto K, Akiyama S, Ueta Y (2017) Estimation of the origin of dissolved organic matter and biogeochemical cycles of nutrients in Osaka Bay, Japan. *J Jpn Soc Water Environ* 40(2):1–9
- Koblinsky CJ, Hildebrand P, LeVine D, Pellerano F, Chao Y, Wilson W, Yueh S, Lagerloef G (2003) Sea surface salinity from space: science goals and measurement approach. *Radio Sci* 38(4):8064. <https://doi.org/10.1029/2001RS002584>
- Kuroda H, Takahashi D, Mitsudera H, Azumaya T, Setou T (2014) A preliminary study to understand the transport process for the eggs and larvae of Japanese Pacific walleye Pollock *Theragra chalcogramma* using particle-tracking experiments based on a high-resolution ocean model. *Fish Sci*. <https://doi.org/10.1007/s12562-014-0717-y>
- Kusaka A, Tomonori Azumaya T, Kawasaki Y (2013) Monthly variations of hydrographic structures and water mass distribution off the Doto area, Japan. *J Oceanogr* 69:295–312. <https://doi.org/10.1007/s10872-013-0174-8>
- Lagerloef GSE, Colomb F, LeVine DM, Wentz F, Yueh S, Ruf C, Lilly J, Gunn J, Chao Y, de Charon A, Feldman G, Swift C (2008) The Aquarius/SAC-D mission: designed to meet the salinity remote-sensing challenge. *Oceanography* 21(1):68–81
- Lee ZP, Carder KL, Arnone RA (2002) Deriving inherent optical properties from water color: a multiband quasi-analytical algorithm for optically deep waters. *Appl Opt* 41(27):5755–5772
- Liu JT, Chao S, Hsu RT (2002) Numerical modeling study of sediment dispersal by a river plume. *Cont Shelf Res* 22:1745–1773
- Molleri GSF, Novo EMLM, Kampel M (2010) Space-time variability of the Amazon River plume based on satellite ocean color. *Cont Shelf Res* 30:342–352. <https://doi.org/10.1016/j.csr.2009.11.015>
- Moon JE, Park YJ, Ryu JH, Choi JK, Ahn JH, Min JE, Son YB, Lee SJ, Han HJ, Ahn YH (2012) Initial validation of GOCI water products against in situ data collected around Korean peninsula for 2010–2011. *Ocean Sci J* 47:261–277. <https://doi.org/10.1007/s12601-012-0027-1>
- Mueller JL, Fargion GS, McClain CR, Pegau S, Mitchell BG, Kahru M, Wieland J, Stramska M (2003) Inherent optical properties: Instruments, characterizations, field measurements and data analysis protocols. NASA technical memorandum, NASA/TM-2003-211621/4(4)
- Nakada S, Isoda Y (2000) Seasonal variation of the Tsushima Warm Current off Toyama Bay. *Umi Sora* 76:17–24 (**in Japanese with English abstract**)
- Nakada S, Ishikawa Y, Awaji T, In T, Shima S, Nakayama T, Isada T, Saitoh S (2012) Modeling runoff into a region of freshwater influence for improved ocean prediction: an application in Funka Bay. *Hydrolo Res Lett* 6:47–52
- Nakada S, Baba K, Sato M, Natsuike M, Ishikawa Y, Awaji T, Koyamada K, Saitoh SI (2014) The role of snowmelt runoff on the ocean environment and scallop production in Funka Bay, Japan. *Progr Earth Planet Sci* 1:25. <https://doi.org/10.3178/HR.L.6.47>
- Nakada S, Hayashi M, Koshimura S, Yoneda S, Kobayashi E (2016) Tsunami-tide simulation in a large bay based on the greatest earthquake scenario along the Nankai Trough. *Int J Offshore Polar Eng* 26(4):392–400
- Nakada S, Hayashi M, Koshimura S, Taniguchi Y, Kobayashi E (2017) Salinization by Tsunami in a semi-enclosed bay: Tsunami-Ocean 3D simulation based on the great earthquake scenario along the Nankai Trough. *J Adv Simul Sci Eng* 3(2):206–214
- Nakajima M (1997) Structure of stratification and changes in water quality of Osaka Bay. *Umi to Sora* 73(1):15–21 (**in Japanese with English abstract**)
- Nelson NB, Siegel DA, Michaels AF (1998) Seasonal dynamics of colored dissolved material in the Sargasso Sea. *Deep-Sea Res I* 45:931–957
- Nelson NB, Siegel DA, Carlson CA, Swan CM (2010) Tracing global biogeochemical cycles and meridional overturning circulation using chromophoric dissolved organic matter. *Geophys Res Lett* 37:L03610. <https://doi.org/10.1029/2009GL042325>
- Qing S, Zhang J, Cui T, Bao Y (2013) Retrieval of sea surface salinity with MERIS and MODIS data in the Bohai Sea. *Remote Sens Environ* 136:117–125. <https://doi.org/10.1016/j.rse.2013.04.016>
- Ryu JH, Han HJ, Cho S, Park YJ, Ahn YH (2012) Overview of geostationary ocean color imager (GOCI) and GOCI data processing system (GDPS). *Ocean Sci J* 47(3):223–233. <https://doi.org/10.1007/s12601-012-0024-4>
- Sakamoto K, Yamanaka G, Tsujino H, Nakano H, Urakawa S, Usui N, Hirabara M, Ogawa K (2016) Development of an operational coastal model of the Seto Inland Sea, Japan. *J Oceanogr* 66:77–97. <https://doi.org/10.1007/s10236-015-0908-9>
- Sasaki H, Siswanto E, Nishiuchi K, Tanaka K, Hasegawa T, Ishizaka J (2008) Mapping the low salinity Changjiang Diluted Water using satellite-retrieved colored dissolved organic matter (CDOM) in the East China Sea during high river flow season. *Geophys Res Lett* 35:L04604. <https://doi.org/10.1029/2007GL032637>
- Senju T, Okuno J, Ookei N, Tsuji T (2013) Behavior of surface low salinity water and mass occurrence of giant jellyfish (*Nemopilema nomurai*) in the coastal area of the Japan Sea in summer 2009. *Umi Sora* 89(2):53–60 (**in Japanese with English abstract**)
- Shigeta T (2008) Recent ecological problems of the fishes in the Seto Inland Sea, Japan. *Nippon Suisan Gakkaishi* 74(5):868–872
- Simpson JH (1997) Physical processes in the ROFI regime. *J Mar Syst* 12:3–15
- Son YB, Gardner WD, Richardson MJ, Ishizaka J, Ryu JH, Kim SH, Lee SH (2012) Tracing offshore low-salinity plumes in the North-eastern Gulf of Mexico during the summer season by use of multi-spectral remote-sensing data. *J Oceanogr* 71:1–19. <https://doi.org/10.1007/s10872-012-0131-y>
- Stedmon CA, Markager S (2005) Tracing the production and degradation of autochthonous fractions of dissolved organic matter by fluorescence analysis. *Limnol Oceanogr* 50(5):1415–1426
- Takagi S, Nanba Y, Fujisawa T, Watanabe Y, Fujiwara T (2012) River-water spread in Bisan Strait with reference to nutrient supply to nori (*Porphyra*) farms. *Bull Jpn Soc Fish Oceanogr* 76(4):197–204 (**in Japanese with English abstract**)
- Twardowski MS, Donaghay PL (2001) Separating in situ and terrigenous sources of absorption by dissolved materials in coastal waters. *J Geophys Res* 106:2545–2560
- Urakawa LS, Kurogi M, Yoshimura K, Hasumi H (2015) Modeling low salinity waters along the coast around Japan using a high-resolution river discharge dataset. *J Oceanogr* 71:715–739. <https://doi.org/10.1007/s10872-015-0314-4>
- Urquhart EA, Zaitchik BF, Hoffman MJ, Guikema SD, Geiger EF (2012) Remotely sensed estimates of surface salinity in the

- Chesapeake Bay: a statistical approach. *Remote Sens Environ* 123:522–531. <https://doi.org/10.1016/j.rse.2012.04.008>
- Vogel RL, Brown CW (2016) Assessing satellite sea surface salinity from ocean color radiometric measurements for coastal hydrodynamic model data assimilation. *J Appl Remote Sens* 10(3):036003. <https://doi.org/10.1117/1.JRS.10.036003>
- Wang M, Tang J, Shi W (2007) MODIS-derived ocean color products along the China east coastal region. *Geophys Res Lett* 34:L06611. <https://doi.org/10.1029/2006GL028599>
- Wouthuyzen S, Tarigan S, Kusmanto E, Supriyadi HI, Sediadi A, Sugarin Siregar VP, Ishizaka J (2011) Measuring sea surface salinity of the Jakarta bay using remotely sensed of ocean color data acquired by modis sensor. *Mar Res Indones* 36(2):51–70
- Yamamoto T, Kitamura T, Matsuda O (1996) Riverine inputs of fresh water, total nitrogen and total phosphorus into the Seto Inland Sea. *J Fac Appl Biol Sci Hiroshima Univ* 35:81–104
- Yanagi T (1980) Variability of the constant flow in Osaka Bay. *J Oceanogr Soc Jpn* 36:252
- Yanagi T (1996) Effects of open ocean variability to the oceanic condition of Osaka Bay and Kii Channel. *Bull Coast Oceanogr* 34(1):53–57 (**in Japanese with English abstract**)
- Yanagi T, Takahashi S (1988a) A tidal front influenced by river discharge. *Dyn Atmos Oceans* 12:191–206
- Yanagi T, Takahashi S (1988b) Response to fresh water discharge in Osaka Bay. *Umi Sola* 64(2):1–8 (**in Japanese with English abstract**)
- Zhu W, Yu Q, Tian YQ, Chen RF, Gardner GB (2011) Estimation of chromophoric dissolved organic matter in the Mississippi and Atchafalaya river plume regions using above-surface hyperspectral remote sensing. *J Geophys Res* 116:C02011. <https://doi.org/10.1029/2010JC006523>